JPhys Energy

PAPER • OPEN ACCESS

Tailoring the orientation of perovskite crystals via adding two-dimensional polymorphs for perovskite solar cells

Journal of Physics: Energy

OPEN ACCESS

RECEIVED
20 February 2020

REVISED
26 April 2020

ACCEPTED FOR PUBLICATION
6 May 2020

PUBLISHED
3 July 2020

PAPER

Tailoring the orientation of perovskite crystals via adding two-dimensional polymorphs for perovskite solar cells

Renjun Guo[1], **Ali Buyruk**[2], **Xinyu Jiang**[1], **Wei Chen**[1], **Lennart K Reb**[1], **Manuel A Scheel**[1], **Tayebeh Ameri**[2] and **Peter Müller-Buschbaum**[1,3,4]

[1] Physik-Department, Lehrstuhl für Funktionelle Materialien, Technische Universität München, James-Franck-Straße 1, Garching, 85748 Germany
[2] Chair of Physical Chemistry, Department of Chemistry, University of Munich (LMU), Butenandtstraße 11 (E), Munich D-81377 Germany
[3] Heinz Maier-Leibnitz-Zentrum, Technische Universität München, Lichtenbergstr, 1, Garching, 85748 Germany
[4] Author to whom any correspondence should be addressed

E-mail: muellerb@ph.tum.de

Keywords: power conversion efficiency yield, morphology, charge carrier dynamics, crystal orientation, perovskite solar cells

Supplementary material for this article is available online

Abstract

Organic-inorganic perovskite materials are attracting increasing attention for their use in high-performance solar cells due to their outstanding properties, such as long diffusion lengths, low recombination rate, and tunable bandgap. Finding an effective method of defect passivation is thought to be a promising route for improvements toward narrowing the distribution of the power conversion efficiency (PCE) values, given by the spread in the PCE over different devices fabricated under identical conditions, for easier commercialization. In this work, we add 2-(4-fluorophenyl)ethyl ammonium iodide (p-f-PEAI) into the bulk of a mixed cation lead halide perovskite $(CH_3NH_3PbBr_3)_{0.15}(HC(NH_2)_2PbI_3)_{0.85}$ thin film. We investigate the influence of different p-f-PEAI concentrations on the optical properties, morphology, crystal orientation, charge carrier dynamics, and device performance. We observe that introducing the proper amount of p-f-PEAI changes the preferential orientation of the perovskite crystals, promotes the strength of the crystal textures, and suppresses non-radiative charge recombination. Thus, we obtain a narrower distribution of the PCE of perovskite solar cells (PSCs) without sacrificing the PCE values reached. This is an important step toward better reproducibility to realize the commercialization of PSCs.

1. Introduction

Today, organic-inorganic halide perovskites are one of the most attractive photovoltaic materials due to their excellent optoelectronic properties and low-temperature fabrication processability [1–5]. The power conversion efficiency (PCE) of single-junction perovskite solar cells (PSCs) started at 3.8% in 2009 and has reached a certified 25.2% in 2019 [6, 7]. Although this tremendous progress has been achieved, the spread in the PCE over different devices fabricated under identical conditions is limiting the potential commercialization of this class of next generation solar cells.

A previous study suggested that the distribution of the PCE of solar cells is related to the recombination process in the bulk, at the grain boundaries and at the interfaces of the light-harvesting layer [8]. Due to being common polycrystalline perovskite films, these films contain substantial structural disorder, such as grain boundary defects and crystallographic defects [9]. From the literature, theoretical studies indicate that trap-assisted defects dominate the distribution of the PCE over different devices under identical conditions, whereas several experiments show that suppressing defects in perovskite films is essential for enhancing the performance of PSCs [10–13].

Mixed cation lead halide perovskites such as $(CH_3NH_3PbBr_3)_{0.15}(HC(NH_2)_2PbI_3)_{0.85}$, denoted $(MAPbBr_3)_{0.15}(FAPbI_3)_{0.85}$ enable PSCs with high efficiency and notable stability, which will both be needed

in real-world devices [14]. Thus, in the present work, we focus on mixed cation lead halide perovskite $(MAPbBr_3)_{0.15}(FAPbI_3)_{0.85}$. Among the routes to improve the PCE distribution in terms of a lower PCE spread, the method of using two-dimensional polymorphs for passivating 3D perovskite films appears very promising [15]. Phenylethylammonium iodide is one of the most important materials in improving the PCE of PSCs [16, 17]. From density functional theory based calculations Zhou *et al* speculated that 2-(4-fluorophenyl)ethyl ammonium iodide (p-f-PEAI) was passivating defects and thereby increasing the device performance [18]. Encouraged by this work, we introduce p-f-PEAI into the bulk of $(MAPbBr_3)_{0.15}(FAPbI_3)_{0.85}$ perovskite films to enhance the distribution of the PCE while maintaining the performance of PSCs in terms of maximum PCE at the same time. When p-f-PEAI reacts with PbI_2 or $PbBr_2$, it forms $(p\text{-}f\text{-}PEAI)_2Pb(I_xBr_{1-x})_4$ which is called a 2D perovskite. In contrast, our original component $(MAPbBr_3)_{0.15}(FAPbI_3)_{0.85}$ is a 3D perovskite. We tune the p-f-PEAI-to-MA/FA mixing ratio by substituting different amounts of MA/FA (fixed at a molar ratio of 0.15:0.85 in the initial solution) with p-f-PEAI cations. We use grazing-incidence wide-angle x-ray scattering (GIWAXS) to analyze the changes in the orientation of doped perovskite crystals caused by adding different amounts of p-f-PEAI [19, 20]. Moreover, we use time-resolved photoluminescence (PL) to investigate the charge carrier dynamics in mixed cation lead halide films with different concentrations of p-f-PEAI [21]. The results show that 3D perovskites doped with p-f-PEAI exhibit not only a stronger preferential orientation of the perovskite structure but also show an improved distribution of the PCE in devices. In the present study, we achieved a champion device efficiency of 18.4% with a substantially improved distribution of the PCE.

2. Experimental section

2.1. Materials

Lead iodide (beads, −10 mesh, 99.999% trace metals basis, product number: 554 359), bis(trifluoromethylsulfonyl)-imide lithium salt (Li-TFSI, product number: 544 094), 4-tert-butylpyridine (TBP, product number: 142 379), chlorobenzene (product number: 284 513), dimethylsulfoxide (DMSO, product number: 276 855), N,N-dimethylformamide (DMF, product number: 227 056), acetonitrile (product number: 271 004), and 2,2′,7,7′-tetrakis-(N,N-di-4-methoxyphenylamine)-9,9′-spirobifluorene (Spiro-OMeTAD, SHT-263 Solarpur, product number: 902 500) were purchased from Sigma-Aldrich. Formamidinium iodide (FAI, product number: MS150000), methylammonium bromide (MABr, product number: MS301000), and tris(2-(1 H-pyrazole-1-yl)-4-tert-butylpyridine)-cobalt(III) tris(bis(trifluoromethylsulfonyl)imide) (FK209) were purchased from Dyesol. Tin(IV) oxide colloid precursor (tin(IV) oxide, 15% in H_2O colloidal dispersion, product number: 44 592–36) was purchased from Alfa Aesar. p-f-PEAI was purchased from Xi'an Polymer Light Technology Corp.

2.2. Device fabrication

2.2.1. Substrate preparation

ITO (15 ohms sqr^{-1}, Lumtec) glass substrates were etched by a diluted HCl solution (deionized (DI) water: HCl solution = 3:1). Before using an ultrasonic bath for 15 min in Hellmanex cleaning solution diluted with DI water in a 2:98 vol vol^{-1} ratio (Sigma-Aldrich, product number: Z805939-1EA), the etched ITO substrates were cleaned by a brush as vigorously as possible but without scratching the ITO surface. After that, we rinsed these ITO glasses with a large amount of DI water. Next, the ITO glasses were put separately into acetone, ethanol, and isopropanol with an ultrasonic bathing procedure for 15 min each, and after that, the glasses were quickly dried with a strong nitrogen gas flow. The substrates were processed further immediately after this cleaning. We often noticed that letting the surface dry in-between the cleaning steps resulted in undesired streaks. For a successful processing, the glass substrate needed to look spotless and free of streaks. All involved cleaning solvents were extra pure or electronic grade quality.

2.2.2. Electron-transport layer fabrication

A diluted SnO_2 solution (raw solution: DI water = 1:3) was spin-coated on pre-plasma cleaned ITO glasses with a speed of 3000 rpm. (acceleration rate 1500 rpm s^{-1}) for 30 s. After that, the films were put on a hotplate at 150 °C for 30 min.

2.2.3. Perovskite layer fabrication

A perovskite precursor solution with lead excess was prepared by dissolving FAI (1.0 M), PbI_2 (1.05 M), MABr (0.2 M), and $PbBr_2$ (0.2 M) in a mixed solvent of anhydrous DMF and DMSO (4:1, volume ratio). After stirring at 70 °C for 30 min, the perovskite precursor was stirred for an additional 30 min at room temperature. We blended the $MA_{0.15}FA_{0.85}Pb(I_{0.85}Br_{0.15})_3$ and p-f-PEAI powder to obtain $p\text{-}f\text{-}PEAI_x(FA_{0.85}\ MA0_{.15})_{1-x}\ Pb(I_{0.85}Br_{0.15})_3$ with the desired p-f-PEAI concentration. The precursors were

spin-coated in a nitrogen-filled glove box. Unlike the procedure described in another publication [22], we used a lower acceleration speed of at 6000 rpm (acceleration rate 750 rpm s^{-1}) for 30 s. Five seconds before the end of the spinning, 120 μl of chlorobenzene (the anti-solvent) was rapidly dropped in the middle of the substrates. Following the spin-coating step, the substrates were placed immediately on a hot plate that had been preheated to 100 °C for 60 min. Before this annealing step, the perovskite films should look semitransparent withe a brown-like-color. After a few minutes on the hot plate, the perovskite films turned opaque black indicating the successful fabrication of the sample.

2.2.4. Hole transport layer fabrication

After the substrates were cooled down to room temperature, 72.3 mg of Spiro-OMeTAD was dissolved in 1 ml of chlorobenzene with additives of 17.5 µl of Li-TFSI solution (520 mg ml^{-1} in acetonitrile), 28.8 µl of TBP, and 8 µl of FK209 solution (180 mg ml^{-1} in acetonitrile). The 50 µl of Spiro-OMeTAD precursor solution was spin-coated on the perovskite layers at 4000 rpm for 30 s. After spin-coating, the substrates were kept in a desiccator with a silica gel (RH < 10%) for 24 h.

2.2.5. Electrode evaporation

An 80 nm gold electrode was thermally evaporated in vacuum (below 2×10^{-5} torr). After that, the substrates were kept in a desiccator with silica gel (RH < 10 %) for a few weeks.

2.2.6. Current–voltage measurements

The *J–V* curves were measured (2611B Series Source Meter, Keithley Instruments) under simulated AM 1.5 sunlight at 100 mW cm^{-2} irradiance generated by a Class ABA sun simulator, with the intensity being calibrated with a calibrated KG–5 filtered Si reference cell (Solar Constant 1200, K.H. Steuernagel Lichttechnik GmbH). The aperture-defined active area of the solar cells was 0.12 cm^{-2}. Both measurements were done at a scan rate of 10 mV s^{-1}. A stabilization time of 10 s at a forward bias of 1.4 V under illumination was performed prior to scanning. We measured eight solar cells for each composition to get statistical device data.

2.2.7. Thin-film characterization

Ultraviolet–visible (UV–vis) absorption spectra were measured using a Lambda 35 (PerkinElmer). Time-resolved photoluminescence (TRPL) spectroscopy was performed with a Picoquant Fluotime 300 spectrofluorometer, using an excitation wavelength of 370 nm. The GIWAXS measurements were performed using an in-house instrument (GANESHA 300 XL SAXS SYSTEM by JJ X-Ray Systems ApS) with the settings: x-ray wavelength = 0.154 nm, incident angle = 0.4°, and sample–detector distance = 95.7 mm. A grazing-incidence x-ray scattering graphical user interface, developed by the Advanced Photon Source (Argonne National Laboratory, USA), was used to reshape the q maps and perform typical corrections [23]. The surface morphology was probed with a field-emission scanning electron microscopy (SEM, Zeiss NVision 40) at an acceleration voltage of 5 kV, a working distance of 2.8 mm, and an aperture size of 10 μm.

3. Results and discussion

Figure 1(a) shows the UV–vis spectra of perovskite films coated on ITO glasses with different doping concentrations including the reference sample (x = 0.00). The concentration of x = 0.02 results in an improved absorption as compared with the reference. Further increasing the amount of the p-f-PEAI increases the absorption for the probed wavelength range [18, 24]. At a concentration of x = 0.08, an absorption peak occurs at around 540 nm due to the formation of the $(p\text{-}f\text{-}PEAI)_2Pb(I_{0.85}Br_{0.15})_4$ phase. The PL spectra of the doped p-f-PEAI films show a redshift of the emission peak wavelength. Compared with the reference sample, it shifts from 760 nm (x = 0.00) to 785 nm (x = 0.08). It is well known that a redshift to 840 nm is beneficial for the light-harvesting of PSCs under AM 1.5 G conditions due to the increasing absorption of sunlight [25]. The formation of the $(p\text{-}f\text{-}PEAI)_2Pb(I_{0.85}Br_{0.15})_4$ phase causes an extended tail-absorption in the near-UV spectrum. However, we did not observe a second PL peak in the steady-state PL spectra corresponding to the peak located at around 540 nm in the absorption spectrum of the sample with the concentration of x = 0.08. The absence of this peak in the PL data could result from strong non-radiative recombination centers in the $(p\text{-}f\text{-}PEAI)_2Pb(I_{0.85}Br_{0.15})_4$ phase so that the hole-electron pairs can recombine immediately after formation.

To evaluate the effect of our passivation strategy on the morphology of the perovskite films, we performed SEM measurements. Figure 2 illustrates the changes in the surface structures for the different p-f-PEAI concentrations. With an increasing amount of p-f-PEAI, the size of the perovskite crystals decreases, and the size distribution narrows. At a concentration of x = 0.08, the distribution of crystal sizes is

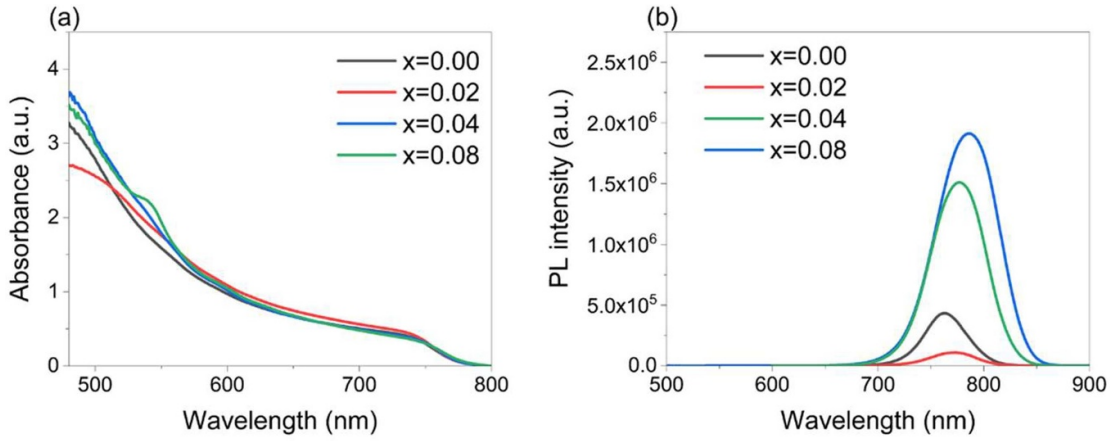

Figure 1. (a) UV–vis spectra and (b) PL spectra of p-f-PEAI doped mixed cation lead halide perovskite $(MAPbBr_3)_{0.15}(FAPbI_3)_{0.85}$ films with concentrations x = 0.00 (black), 0.02 (red), 0.04 (blue), and 0.08 (green).

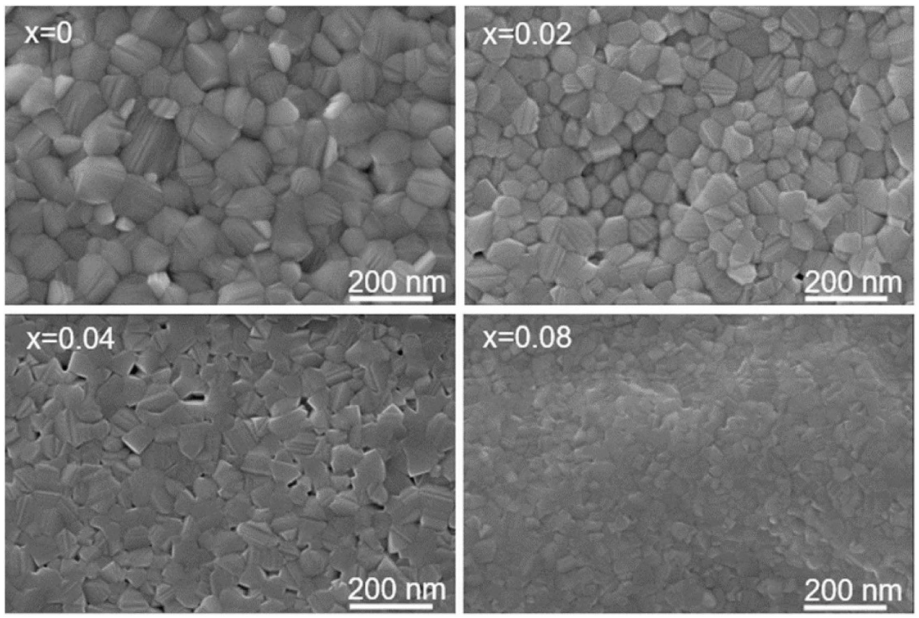

Figure 2. SEM images showing the surface structures of post-annealed films with different p-f-PEAI concentrations as indicated, grown on ITO substrates.

the narrowest, showing that adding p-f-PEAI is beneficial for homogenizing the crystal sizes. The real grain structure shows a dense, pinhole-free morphology for all films. The statistical grain size distribution is shown in figure S1 avaliable online at stacks.iop.org/JPENERGY/2/034005/mmedia.

To investigate the structural changes in the different perovskite films and to confirm the formation of $(p\text{-f-PEAI})_2Pb(I_{0.85}Br_{0.15})_4$ phases with increasing the amount of p-f-PEAI, we characterize the perovskite films with GIWAXS [26–29]. Figures 3(a)–(d) show the reshaped and corrected 2D GIWAXS data. For further analysis, an azimuthal integration of the 2D GIWAXS data was done. The resulting data are shown in figure 3(e). At a concentration of x = 0.08, the formed $(p\text{-f-PEAI})_2Pb(I_{0.85}Br_{0.15})_4$ phase is well visible at $q = 0.3\ nm^{-1}$. In contrast, at lower concentrations the scattering data does not show the Bragg peaks of the 2D perovskite. As seen in the tube cuts of the (001) perovskite, the Bragg peak from the 2D GIWAXS data, and the corresponding Gaussian fits (figure 3(f)), an extremely small amount of p-f-PEAI can already result in the formation of a new face-on texture for the cubic phase of perovskite films. Thus, parts of the crystals have (001) crystal planes oriented parallel to the substrate, while the original edge-on texture component still persists. Therefore, the addition of p-f-PEAI can change the preferential orientation of perovskite crystals inside the film but still maintains the original texture. With increasing amount of p-f-PEAI, the preferential textures of the (001) Bragg peaks of the perovskite films do not change anymore, while the strength of both the edge-on and face-on preferential orientation increases.

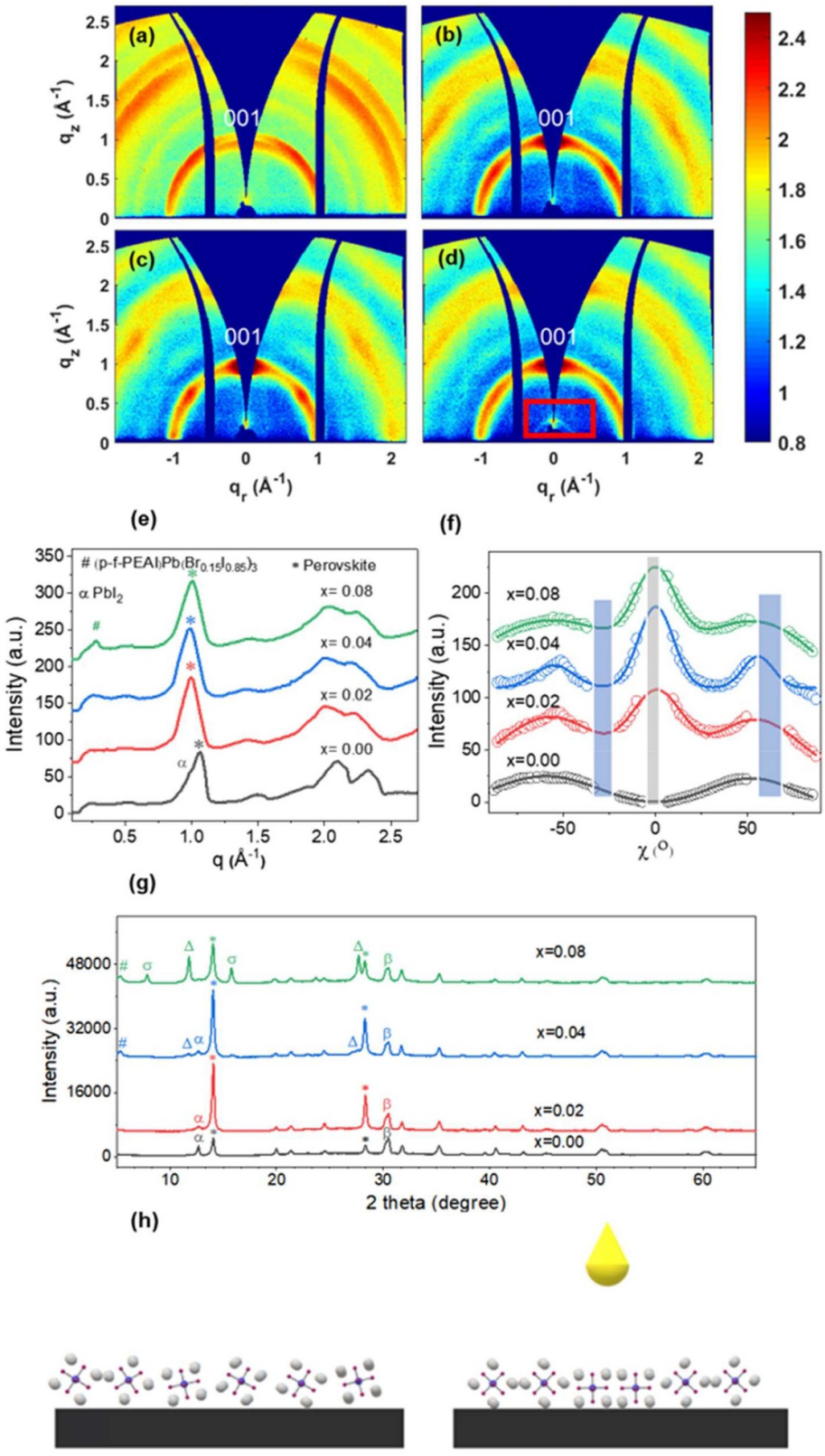

Figure 3. (a)–(d) 2D GIWAXS data of the perovskite films with different p-f-PEAI concentrations of x = 0.00 (a), 0.02 (b), 0.04 (c), 0.08 (d). (e) Azimuthal integrals from the 2D GIWAXS data for different p-f-PEAI concentrations x. Characteristic Bragg peaks of the 3D perovskite (star), PbI_2 (alpha), and of $(p\text{-f-PEAI})_2Pb(I_{0.85}Br_{0.15})_4$ (number sign) are highlighted. (f) Tube cuts of the (001) perovskite Bragg peak from the 2D GIWAXS data (symbols) and corresponding fits with Gaussian functions (solid line) for different p-f-PEAI concentrations x. Blue columns mark detector gaps and the grey column is the missing wedge. (g) XRD data of the perovskite films with different p-f-PEAI concentrations. Characteristic Bragg peaks of the $(p\text{-f-PEAI})_2Pb(I_{0.85}Br_{0.15})_4$ (number sign), intermediate phases (sigma and delta), PbI_2 (alpha), 3D perovskite (star), and ITO (beta) are highlighted. (h) Schematic diagram depicting the orientation the of the perovskite phase in the reference film (x = 0.00) and in the films with added p-f-PEAI.

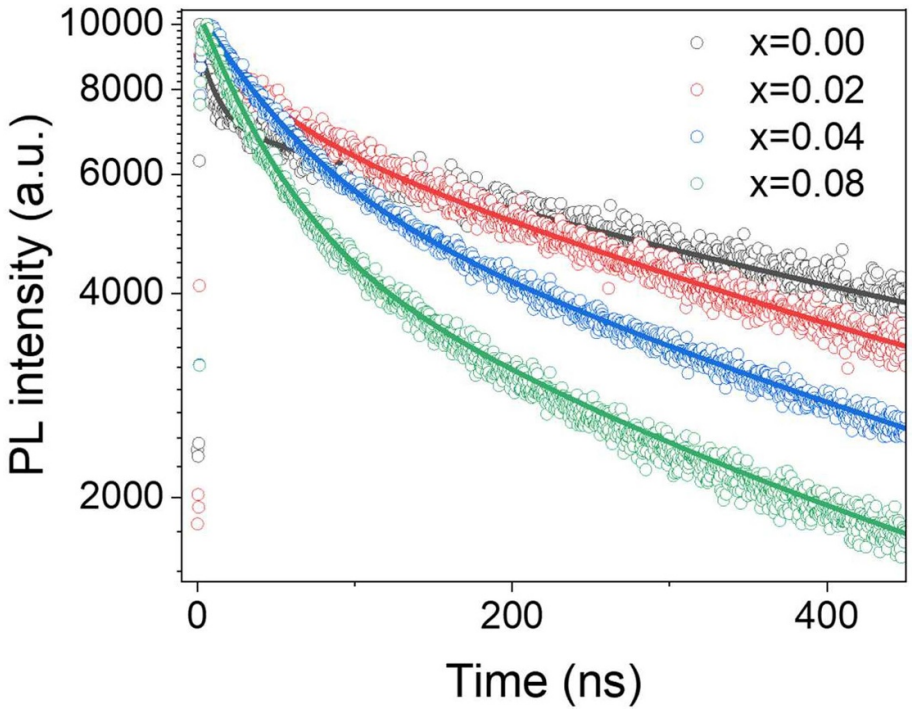

Figure 4. Time-resolved PL probed at 763, 773, 787, and 777 nm for perovskite films with p-f-PEAI concentrations of x = 0.00 (black), 0.02 (red), 0.04 (blue), and 0.08 (green), respectively and corresponding fits based on a two-phase exponential decay (lines).

Table 1. Parameters from fits to the TRPL data of doped perovskite films using a two-phase exponential decay (equation (2)).

Sample	A_1 (%)	τ_1 (ns)	A_2 (%)	τ_2 (ns)
x = 0	24	11.6 ± 0.6	76	503.5 ± 6.4
x = 0.02	24.5	40.9 ± 1.4	75.5	408.0 ± 5.3
x = 0.04	41.6	53.6 ± 0.6	59.4	391.6 ± 3.7
x = 0.08	54.6	41.7 ± 0.4	45.4	301.9 ± 3.0

The x-ray diffraction (XRD) data confirms the consumption of excess PbI_2 due to the addition of p-f-PEAI as well as the formation of a 2D perovskite phase with increasing the amount of p-f-PEAI (figure 3(g)). Compared with the undoped perovskite film, the intensity of the PbI_2 (001) peak (located at 2theta = 12.6°) decreases strongly with increasing the amount of p-f PEAI. For the perovskite films with concentrations x = 0.02 and x = 0.04 the PbI_2 phase still exists. For the films with a ratio of concentrations of x = 0.04 and 0.08, the scattering peaks of the 2D perovskite phase (#) and two related uncertain intermediate phases (sigma and delta) can be found as already reported in the literature [18, 24]. Figure 3(h) shows the crystal orientation modification by adding p-f-PEAI. In contrast to the mostly random with slightly preferred edge-on orientation distribution for the concentration of x = 0.00, the crystal tends to preferentially align in plane when p-f-PEAI is added. We note that the sketched unit cells in figure 3(h) just schematically depict the crystal orientation rather than the true crystal grain sizes.

An understanding of what governs charge-carrier recombination is highly crucial as recombination competes with an efficient charge collection in the solar cells. In order to study the charge carrier dynamics of different p-f-PEAI concentrations used for doping the perovskite films, we performed TRPL measurements for perovskite films on glass substrates. The results are shown in figure 4. In general, there are three underlying recombination mechanisms in perovskite materials, which are radiative recombination, Shockley–Read–Hall recombination, Auger recombination, and surface recombination [30]. A range of different recombination mechanisms is expressed via

$$\frac{dn}{dt} = -k_1 n - k_2 n^2 - k_3 n^3 \quad (1)$$

where n is the charge-carrier density, k_1 is typically related to monomolecular recombination, k_2 is related to bimolecular recombination, and k_3 is the Auger recombination constant [31, 32]. We use a two-phase

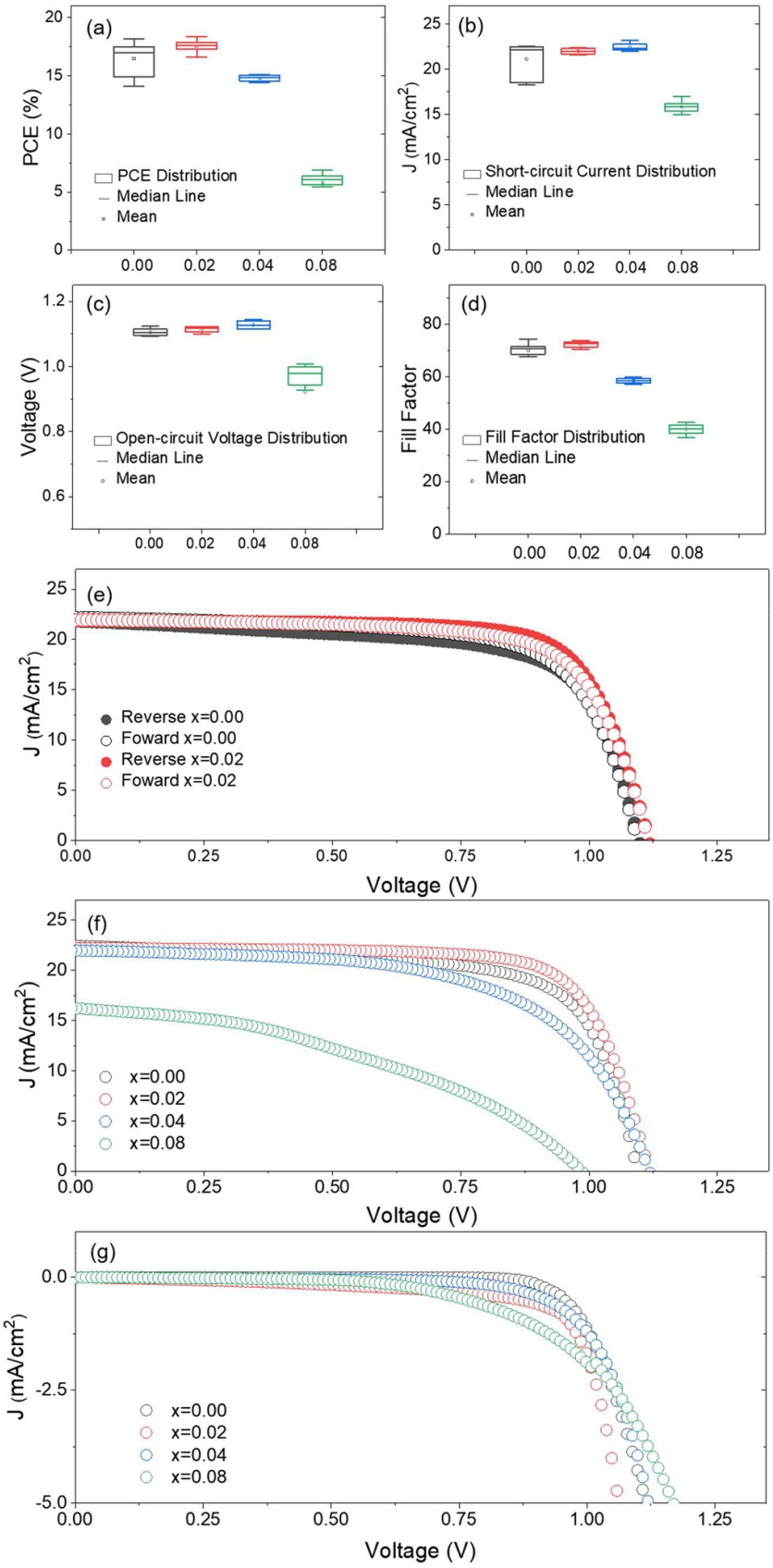

Figure 5. (a)–(d) Solar cell parameters from the *J–V* characterization of (a) PCE, (b) J_{sc}, (c) V_{oc}, and FF (d) of PSCs fabricated with different p-f-PEAI concentrations. (e) Hysteresis behavior of PSCs with different concentrations of p-f-PEAI doping (x = 0.00 and 0.02). (f) *J–V* curves of champion devices and (g) dark *J–V* curves with different concentrations of p-f-PEAI doping (x = 0.00, 0.02, 0.04, and 0.08).

Table 2. Device parameters of PSCs with different concentrations of p-f-PEAI doping.

Sample	V_{oc}	J_{sc}	Fill Factor	PCE
x = 0.00	1.10 ± 0.01	21.1 ± 1.9	70.1 ± 2.8	16.5 ± 1.5
x = 0.02	1.11 ± 0.01	22.0 ± 0.4	72.4 ± 1.3	17.7 ± 0.6
x = 0.04	1.13 ± 0.01	22.4 ± 0.5	58.5 ± 1.1	14.8 ± 0.3
x = 0.08	0.92 ± 0.16	15.8 ± 0.6	40.0 ± 2.2	5.8 ± 1.0

exponential decay function with a time offset (t_0 is fixed at the highest intensity point, y_0 is the offset of data) which has been used before in previous publications to fit TRPL data [33]

$$y = y_0 + A_1 e^{\frac{-(t-t_0)}{\tau_1}} + A_2 e^{\frac{-(t-t_0)}{\tau_2}} \quad . \tag{2}$$

The results are summarized in table 1. We attribute the recombination mechanism of the fast decay component (τ_1) to a fast energy transport (such as a charge carrier quench), while the slower decay component could be related to a radiative recombination (τ_2) [34, 35]. Comparing the pristine perovskite film with the p-f-PEAI doped perovskite film, we can deduce from an increased τ_1 that p-f-PEAI could decrease the charge carrier quenching effect significantly. A quench-reduced bulk layer can contribute to a higher photocurrent in the potential device. However, as a side effect, the insulating nature of p-f-PEAI and the p-f-PEAI related perovskite phases increase the number of non-radiative recombination centers in the perovskite layer, as seen from a decreased value of τ_2. Thus, we observe a trade-off process by adding different concentrations of p-f-PEAI into the perovskite solution. In the overall weighting metric, the x = 0.02 sample exhibits an apparently improved carrier dynamic, which is in a good agreement with the corresponding device performance as seen in figure 5(f).

To probe the impact of different p-f-PEAI concentrations on the performance of the PSCs, we fabricated devices with a functional stack as ITO/SnO_2/perovskite/Spiro-OMeTAD/Au. Figures 5(a)–(d) illustrate an enhancement of the distribution of the PCE for the PSCs after adding p-f-PEAI with the concentration of x = 0.02. The improved results are mainly from short-circuit current increases due to the suppression of the carrier quenching effect, and from a narrowing of the distribution of the short-circuit current. Simultaneously, the open-circuit voltage and the fill factor are improved slightly. Due to these reasons, the maximum PCE of 18.4% is achieved for the device with a concentration of x = 0.02 which has J_{SC} = 22.25 mA cm^{-2}, V_{OC} = 1.12 V, and FF = 0.74. At concentrations of x = 0.04 and x = 0.08, the formation of insulating 2D perovskite phases and related intermediate phases in the PSCs could harm the charge carrier separation process due to their high binding energy compared to pristine 3D perovskite [36]. We minimized the hysteresis behavior of our reference and doped PSCs by using SnO_2 as the electron transport layer (figure 5(e)). Figure 5(f) illustrates how the *J–V* curves of the respective champion devices for the different concentrations of p-f-PEAI. Figure 5(g) shows the dark *J–V* curves of PSCs with different concentrations of p-f-PEAI doping and table 2 provides the device parameters of the solar cells.

With the above observations, we show that the surface morphology of perovskite films can be modified by adding p-f-PEAI. In addition, a small amount of p-f-PEAI doping can not only slightly improve the light absorption of perovskite film in terms of the AM 1.5 spectrum, but also can dramatically change the preferred crystal orientation while maintaining the original crystal texture. Also, the addition of p-f-PEAI can enhance the texture strength. However, with an increasing amount of p-f-PEAI, the texture seen in the (001) Bragg peak of perovskite films does not change anymore, while the strength of both the edge-on and face-on preferential orientation increases. Hence, we deduce that the formation of a new texture is not the only reason for the improvement in the electrical properties. Recently, Zheng *et al* proposed that the promotion of a (100) texture strength occurred, restricting the grains' tilt during growth and eventually resulted in a (100)-orientation-dominant film that is of lower defect density than a randomly oriented film [37]. An excess of PbI_2 can enhance the electronic quality of perovskite film [38, 39]. Thus, charge carrier quenching of perovskite film is suppressed at a concentration of x = 0.02 due to the passivation effect of doping with p-f-PEAI and PbI_2. The observed improvements in the light absorption and the carrier quenching are passivated when we continue to increase the ratio of p-f-PEAI to concentrations of x = 0.04 and x = 0.08, but $(p\text{-}f\text{-}PEAI)_2Pb(I_{0.85}Br_{0.15})_4$ crystals form, as seen in the XRD data (at 5° in figure 3(g)). At the p-f-PEAI concentrations of x = 0.04 and x = 0.08 in the perovskite films, the $(p\text{-}f\text{-}PEAI)_2Pb(I_{0.85}Br_{0.15})_4$ and relative intermediate phases coexist. The insulating nature of the p-f-PEAI related perovskite phases could be a barrier for the charge separation process in a real device. Thus, the performance of real devices for concentrations of x = 0.04 and x = 0.08 decreases. In addition, non-radiative recombination increases with increasing the amount of the p-f-PEAI and the p-f-PEAI related phases. Therefore, the best performance of

the device with a concentration of x = 0.02 seems to be a result of the interplay between p-f-PEAI-induced passivation of deep traps, stronger textures, and the presence of excess PbI_2.

4. Conclusion

To conclude, we have revealed that, by adding different concentrations of p-f-PEAI, a new face-on texture of the cubic phase of perovskite films forms, and also the texture strength is enhanced. TRPL measurements indicate that there is a trade-off process for the p-f-PEAI doping of perovskite materials regarding the charge carrier dynamics. We speculate that the change in the morphology and texture strength, due to the doping with p-f PEAI, seems to suppress the charge carrier quenching effect and is beneficial for the charge extraction. Furthermore, by well regulating the p-f-PEAI content, we improved the PCE distribution in terms of a lower PCE spread of PSCs without sacrificing the achievable PCE. Therefore, the promotion of texture strength could affect the charge-carrier dynamics of perovskite films. Equally importantly, we have shown an important step toward the production of PSCs, which have both a high and reproducible PCE at the same time. Such developments are necessary to realize real-world applications. We believe that this will have an impact on the continuing developments in perovskite-related optoelectronic devices, and pave the way to further understand the structure dependent material properties and develop theoretical models.

Acknowledgments

Financial support from Deutsche Forschungsgemeinschaft (DFG, German Research Foundation) under Germany's Excellence Strategy—EXC 2089/1–390776260 (e-conversion) as well as from TUM.solar in the context of the Bavarian Collaborative Research Project Solar Technologies Go Hybrid (SolTech) is acknowledged. R G, X J and W C thank for the financial support from the Chinese Scholarship Council (CSC).

ORCID iDs

Renjun Guo https://orcid.org/0000-0003-1116-3334
Xinyu Jiang https://orcid.org/0000-0003-2580-9431
Wei Chen https://orcid.org/0000-0001-9550-0523
Lennart K Reb https://orcid.org/0000-0003-2838-9276
Manuel A Scheel https://orcid.org/0000-0003-0508-6694
Tayebeh Ameri https://orcid.org/0000-0002-8928-3697
Peter Müller-Buschbaum https://orcid.org/0000-0002-9566-6088

References

[1] Green M A, Ho-Baillie A and Snaith H J 2014 The emergence of perovskite solar cells *Nat. Photon.* **8** 506
[2] Bi Y, Hutter E M, Fang Y, Dong Q, Huang J and Savenije T J 2016 Charge carrier lifetimes exceeding 15 μs in methylammonium lead iodide single crystals *J. Phys. Chem. Lett.* **7** 923–8
[3] Stranks S D, Eperon G E, Grancini G, Menelaou C, Alcocer M J, Leijtens T, Herz L M, Petrozza A and Snaith H J 2013 Electron-hole diffusion lengths exceeding 1 micrometer in an organometal trihalide perovskite absorber *Science* **342** 341–4
[4] Dong Q, Fang Y, Shao Y, Mulligan P, Qiu J, Cao L and Huang J 2015 Electron-hole diffusion lengths >175 μm in solution-grown $CH_3NH_3PbI_3$ single crystals *Science* **347** 967–70
[5] De Wolf S, Holovsky J, Moon S-J, Löper P, Niesen B, Ledinsky M, Haug F-J, Yum J-H and Ballif C 2014 Organometallic halide perovskites: sharp optical absorption edge and its relation to photovoltaic performance *J. Phys. Chem. Lett.* **5** 1035–9
[6] Kojima A, Teshima K, Shirai Y and Miyasaka T 2009 Organometal halide perovskites as visible-light sensitizers for photovoltaic cells *J. Am. Chem. Soc.* **131** 6050–1
[7] Green M A, Dunlop E D, Hohl-Ebinger J, Yoshita M, Kopidakis N and Ho-Baillie A W 2020 Solar cell efficiency tables (Version 55) *Prog. Photovoltaics Res. Appl.* **28** 3–15
[8] Wetzelaer G J A, Scheepers M, Sempere A M, Momblona C, Ávila J and Bolink H J 2015 Trap-assisted non-radiative recombination in organic–inorganic perovskite solar cells *Adv. Mater.* **27** 1837–41
[9] Buin A, Pietsch P, Xu J, Voznyy O, Ip A H, Comin R and Sargent E H 2014 Materials processing routes to trap-free halide perovskites *Nano Lett.* **14** 6281–6
[10] Tan H, Jain A, Voznyy O, Lan X, de Arquer F P G, Fan J Z, Quintero-Bermudez R, Yuan M, Zhang B and Zhao Y 2017 Efficient and stable solution-processed planar perovskite solar cells via contact passivation *Science* **355** 722–6
[11] Yang W S, Park B-W, Jung E H, Jeon N J, Kim Y C, Lee D U, Shin S S, Seo J, Kim E K and Noh J H 2017 Iodide management in formamidinium-lead-halide–based perovskite layers for efficient solar cells *Science* **356** 1376–9
[12] Zou Y, Cui Y, Wang H-Y, Cai Q, Mu C and Zhang J-P 2019 Highly efficient and stable 2D–3D perovskite solar cells fabricated by interfacial modification *Nanotechnology* **30** 275202
[13] Abdi-Jalebi M, Andaji-Garmaroudi Z, Cacovich S, Stavrakas C, Philippe B, Richter J M, Alsari M, Booker E P, Hutter E M and Pearson A J 2018 Maximizing and stabilizing luminescence from halide perovskites with potassium passivation *Nature* **555** 497–501

[14] Bi D, Tress W, Dar M I, Gao P, Luo J, Renevier C, Schenk K, Abate A, Giordano F and Baena J-P C 2016 Efficient luminescent solar cells based on tailored mixed-cation perovskites *Sci. Adv.* **2** e1501170
[15] Yoo H-S and Park N-G 2018 Post-treatment of perovskite film with phenylalkylammonium iodide for hysteresis-less perovskite solar cells *Sol. Energy Mater. Sol. Cells* **179** 57–65
[16] Jiang Q, Zhao Y, Zhang X, Yang X, Chen Y, Chu Z, Ye Q, Li X, Yin Z and You J 2019 Surface passivation of perovskite film for efficient solar cells *Nat. Photon.* **13** 460–6
[17] Li M H, Yeh H H, Chiang Y H, Jeng U S, Su C J, Shiu H W, Hsu Y J, Kosugi N, Ohigashi T and Chen Y A 2018 Highly efficient 2D/3D hybrid perovskite solar cells via low-pressure vapor-assisted solution process *Adv. Mater.* **30** 1801401
[18] Zhou Q, Liang L, Hu J, Cao B, Yang L, Wu T, Li X, Zhang B and Gao P 2019 High-performance perovskite solar cells with enhanced environmental stability based on a (p-$FC_6H_4C_2H_4NH_3$) 2 [PbI_4] capping layer *Adv. Energy Mater.* **9** 1802595
[19] Müller-Buschbaum P 2014 The active layer morphology of organic solar cells probed with grazing incidence scattering techniques *Adv. Mater.* **26** 7692–709
[20] Schlipf J, Docampo P, Schaffer C J, Körstgens V, Bießmann L, Hanusch F, Giesbrecht N, Bernstorff S, Bein T and Müller-Buschbaum P 2015 A closer look into two-step perovskite conversion with X-ray scattering *J. Phys. Chem. Lett.* **6** 1265–9
[21] Hu Y, Hutter E M, Rieder P, Grill I, Hanisch J, Aygüler M F, Hufnagel A G, Handloser M, Bein T and Hartschuh A 2018 Understanding the role of cesium and rubidium additives in perovskite solar cells: trap states, charge transport, and recombination *Adv. Energy Mater.* **8** 1703057
[22] Saliba M, Correa-Baena J-P, Wolff C M, Stolterfoht M, Phung N, Albrecht S, Neher D and Abate A 2018 How to make over 20% efficient perovskite solar cells in regular (n–i–p) and inverted (p–i–n) architectures *Chem. Mater.* **30** 4193–201
[23] Jiang Z 2015 GIXSGUI: a MATLAB toolbox for grazing-incidence X-ray scattering data visualization and reduction, and indexing of buried three-dimensional periodic nanostructured films *J. Appl. Crystallogr.* **48** 917–26
[24] Wang Z, Lin Q, Chmiel F P, Sakai N, Herz L M and Snaith H J 2017 Efficient ambient-air-stable solar cells with 2D–3D heterostructured butylammonium-caesium-formamidinium lead halide perovskites *Nat. Energy* **2** 17135
[25] Min H, Kim M, Lee S-U, Kim H, Kim G, Choi K, Lee J H and Seok S I 2019 Efficient, stable solar cells by using inherent bandgap of α-phase formamidinium lead iodide *Science* **366** 749–53
[26] Chen W *et al* 2019 Structure and charge carrier dynamics in colloidal PbS quantum dot solids *J. Phys. Chem. Lett.* **10** 2058–65
[27] Schlipf J and Müller-Buschbaum P 2017 Structure of organometal halide perovskite films as determined with grazing-incidence x-ray scattering methods *Adv. Energy Mater.* **7** 1700131
[28] Oesinghaus L, Schlipf J, Giesbrecht N, Song L, Hu Y, Bein T, Docampo P and Müller-Buschbaum P 2016 Toward tailored film morphologies: the origin of crystal orientation in hybrid perovskite thin films *Adv. Mater. Interfaces* **3** 1600403
[29] Schlipf J, Hu Y, Pratap S, Bießmann L, Hohn N, Porcar L, Bein T, Docampo P and Müller-Buschbaum P 2019 Shedding light on the moisture stability of 3D/2D hybrid perovskite heterojunction thin films *ACS Appl. Energy Mater.* **2** 1011–18
[30] Volovichev I, Logvinov G, Titov O Y and Gurevich Y G 2004 Recombination and lifetimes of charge carriers in semiconductors *J. Phys. D: Appl. Phys.* **95** 4494–6
[31] Herz L M 2016 Charge-carrier dynamics in organic-inorganic metal halide perovskites *Annu. Rev. Phys. Chem.* **67** 65–89
[32] Johnston M B and Herz L M 2015 Hybrid perovskites for photovoltaics: charge-carrier recombination, diffusion, and radiative efficiencies *Acc. Chem. Res.* **49** 146–54
[33] Tang H, Zhong J, Chen W, Shi K, Mei G, Zhang Y, Wen Z, Müller-Buschbaum P, Wu D and Wang K 2019 Lead sulfide quantum dot photodetector with enhanced responsivity through a two-step ligand-exchange method *ACS Appl. Nano Mater.* **2** 6135–43
[34] Liang P W, Liao C Y, Chueh C C, Zuo F, Williams S T, Xin X K, Lin J and Jen A K 2014 Additive enhanced crystallization of solution-processed perovskite for highly efficient planar-heterojunction solar cells *Adv. Mater.* **26** 3748–54
[35] Chen Q, Zhou H, Song T B, Luo S, Hong Z, Duan H S, Dou L, Liu Y and Yang Y 2014 Controllable self-induced passivation of hybrid lead iodide perovskites toward high performance solar cells *Nano Lett.* **14** 4158–63
[36] Blancon J-C, Stier A V, Tsai H, Nie W, Stoumpos C C, Traore B, Pedesseau L, Kepenekian M, Katsutani F and Noe G 2018 Scaling law for excitons in 2D perovskite quantum wells *Nat. Commun.* **9** 1–10
[37] Zheng X, Hou Y, Bao C, Yin J, Yuan F, Huang Z, Song K, Liu J, Troughton J and Gasparini N 2020 Managing grains and interfaces via ligand anchoring enables 22.3%-efficiency inverted perovskite solar cells *Nat. Energy* **5** 131–40
[38] Jacobsson T J, Correa-Baena J-P, Halvani Anaraki E, Philippe B, Stranks S D, Bouduban M E, Tress W, Schenk K, Teuscher J and Moser J-E 2016 Unreacted PbI2 as a double-edged sword for enhancing the performance of perovskite solar cells *J. Am. Chem. Soc.* **138** 10331–43
[39] Jiang Q, Chu Z, Wang P, Yang X, Liu H, Wang Y, Yin Z, Wu J, Zhang X and You J 2017 Planar-structure perovskite solar cells with efficiency beyond 21% *Adv. Mater.* 29 1703852